

X-ray natural circular dichroism and chiral-EXAFS in gyrotropic crystals

José Goulon,^{a*} Chantal Goulon-Ginet,^{a,b} Andrei Rogalev,^a Gisèle Benayoun,^a Christian Brouder^c and Calogero R. Natoli^d

^aEuropean Synchrotron Radiation Facility, BP 220, F-38043 Grenoble CEDEX, France,

^bUniversité Joseph Fourier, Faculté de Pharmacie, Domaine de la Merci, F-38700 La Tronche,

France, ^cLaboratoire de Minéralogie-Cristallographie, Universités de Paris VI et VII, Case 115,

Associé au CNRS, 4 place Jussieu, F-75252 Paris CEDEX 05, France, and ^dLaboratori

Nazionali di Frascati dell'Istituto di Fisica Nucleare, PO Box 13, I-00044 Frascati, Italy.

E-mail: goulon@esrf.fr

(Received 7 February 2000; accepted 23 February 2000)

X-ray natural circular dichroism (XNCD) has been recently detected in the XANES region for uniaxial and biaxial gyrotropic crystals. Chiral-EXAFS (χ -EXAFS) spectra are reported for the first time over a wider energy range and are analysed in terms of multiple-scattering paths of relevant symmetry. For such heavily absorbing single crystals as lithium iodate, paratellurite or potassium titanyl phosphate, the differential absorption between left-handed and right-handed circularly polarized X-ray photons cannot be measured in transmission but gyrotropy effects can still be detected in fluorescence excitation spectra. Whereas XNCD and fluorescence-detected X-ray natural circular dichroism spectra are strictly identical for uniaxial crystals, it has been established that this was true only to the first order for biaxial crystals such as potassium titanyl phosphate.

Keywords: optical activity; gyrotropy; XNCD; χ -EXAFS.

1. Introduction

Since the discovery by Arago and Biot that crystalline quartz induces a rotation of the polarization vector of linearly polarized light (Arago, 1811; Biot, 1812), the optical activity of single crystals has fascinated many successive generations of physicists. It is, however, only in these very recent years that X-ray natural circular dichroism (XNCD) was unambiguously detected in gyrotropic crystals (Goulon, Goulon-Ginet *et al.*, 1998; Goulon *et al.*, 1999a; Alagna *et al.* 1998; Stewart *et al.*, 1999). Such pioneering experiments, which were performed about 100 years after the discovery of X-rays (Röntgen, 1896) and of circular dichroism in the visible (Cotton, 1895), became feasible due to the recent availability of intense beams of circularly polarized X-rays at third-generation synchrotron radiation sources. It has been known for many years that optical activity can be observed exclusively in non-centrosymmetrical crystals but let us recall that only a restricted number of non-centrosymmetrical crystal classes are suitable for detecting XNCD. Looking for the rotational invariants of the rank-3 optical activity tensor γ_{ijk} in O_3^+ , one is led to decompose it into a scalar part, a vector part and a rank-2 pseudo-deviator part (Jerphagnon & Chemla, 1976). At optical wavelengths, both the pseudo-scalar term and the pseudo-deviator part contribute to a sizeable optical activity, whereas, in the X-ray range, only the

pseudo-deviator part will contribute to XNCD (Goulon, Goulon-Ginet *et al.*, 1998; Goulon *et al.*, 1999a). This is because the origin of optical activity is fairly different in optical or in inner-shell spectroscopies.

(i) In optical spectroscopy the Rosenfeld–Condon rotatory strength refers to the interference term $E1.M1$ involving the electric ($E1$) and magnetic ($M1$) dipole matrix elements. The pseudo-scalar nature of this term makes it possible to detect circular dichroism or optical rotation in powdered samples or in solution as well as in single crystals.

(ii) For inner-shell spectroscopies, magnetic dipole transitions ($M1$) are forbidden due to the orthogonality of the core and valence orbitals ($\Delta n = 0$ selection rule). This argument is even more restrictive for spectra recorded at the K or L_1 edges because no magnetic dipole transition is allowed from a fully symmetrical $1s$ or $2s$ atomic state, while the energy separation between $1s$, $2p$ levels makes hybridization quite improbable. However, as pointed out a long time ago (Goulon, 1990), the traceless tensor resulting from the interference between the electric dipole and electric quadrupole $E1.E2$ can also contribute to optical activity in the X-ray range. This was confirmed by more recent theories (Natoli *et al.*, 1998; Okutani *et al.*, 1999). The contribution of the latter terms to optical activity in the visible range is expected to be very small but it was first investigated by Barron in the early 1970s (Barron, 1971). Since the interference tensor $E1.E2$ is traceless, there is a

priori no hope of detecting any large XNCD signal in powdered sample nor in solution in which there is no orientational order.

We have summarized in Table 1 which ones of the 21 non-centrosymmetrical classes are suitable for detecting XNCD. Note that there are two crystal classes (432; 23) which have a non-zero pseudo-scalar term but no pseudo-deviator term: even though such crystals are optically active at optical wavelengths, they cannot exhibit any detectable XNCD as confirmed experimentally. Thus, only 13 crystal classes are compatible with XNCD: all of them can be predicted to have a significant non-linear susceptibility at optical wavelengths and the crystals belonging to these classes are quite often used for second-harmonic generation (SHG) with lasers.

The first results which we will review concern uniaxial crystals of lithium iodate (α -LiIO₃) and paratellurite (α -TeO₂) which belong to the enantiomorphous crystal classes 3 and 422, respectively.

A far more delicate study concerned a biaxial crystal of KTP (potassium titanyl phosphate: KTiOPO₄) which belongs to the non-enantiomorphous crystal class *mm2* so that one cannot isolate a crystal with either a left-handed or a right-handed chirality. As pointed out by Thomas *et al.* (1991), the symmetry requirements of the point group *mm2* dictate that there cannot be any gyration along the optical axes of this crystal but a significant gyration with opposite sign is expected along the [120] and $[\bar{1}\bar{2}0]$ directions of propagation of the incident X-ray beam.

From the experimental point of view, such crystals are heavily absorbing in the X-ray range of interest and circular dichroism cannot be measured in a trivial transmission geometry. This difficulty can, however, be overcome by measuring fluorescence-detected XNCD spectra, hereafter denoted 'Fd-XNCD' spectra. As discussed in §2, it can be established that XNCD and Fd-XNCD spectra are strictly proportional for uniaxial crystals but this is only true to the first order for biaxial crystals such as KTP. The formulation required to simulate XNCD and χ -EXAFS spectra in the general framework of multiple-scattering wave calculations is also detailed. Further experimental aspects regarding biaxial crystals are also briefly envisaged before the presentation of the XNCD spectra in §3.

2. Formulation of XNCD and Fd-XNCD spectra

2.1. Stokes vector in anisotropic absorbing media

The easiest way to introduce the concept of gyrotropy in anisotropic media is by adapting the theory of refringent scattering to the X-ray range. For a transverse polarized wave propagating along the direction n_γ , the complex scattering tensor $a_{\alpha\beta}^*$ can be expanded as

$$a_{\alpha\beta}^* = \alpha_{\alpha\beta}^* + \zeta_{\alpha\beta\gamma}^* n_\gamma + Q_{\alpha\gamma\beta}^* [n_\gamma^2] + \dots, \quad (1)$$

with $\alpha, \beta \neq \gamma$. In (1), $\alpha_{\alpha\beta}^*$ and $Q_{\alpha\gamma\beta}^*$ are the well known electric dipole and electric quadrupole complex polarizability tensors. Much less familiar to X-ray spectroscopists

Table 1

Rotational invariants of γ_{ijk} for the 21 non-centrosymmetrical crystal classes.

Crystal classes	Point groups	Enantiomorphism		XNCD
		Pseudo-scalar	Vector	
$\bar{4}3m$ $\bar{6}m\bar{6}$	T_d D_{3h} C_{3h}	No	No	No
432 23	O T	Yes	No	No
622 32 422	D_6 D_3 D_4	Yes	No	Yes
$6mm$ $3m$ $4mm$	C_{6v} C_{3v} C_{4v}	No	Yes	No
6 3 4	C_6 C_3 C_4	Yes	Yes	Yes
$\bar{4}2m$	D_{2d}	No	No	Yes
4	S_4	No	No	Yes
$mm2$	C_{2v}	No	Yes	Yes
222	D_2	Yes	No	Yes
2	C_2	Yes	Yes	Yes
m	C_s	No	Yes	Yes
1	C_1	Yes	Yes	Yes

is the contribution of the complex gyrotropy tensor $\zeta_{\alpha\beta\gamma}^*$ which is responsible for optical activity. Inside the crystal the variation of the Stokes vector $|\mathbf{S}\rangle$ with the penetration depth z is determined by the differential equation

$$\frac{\partial |\mathbf{S}(z)\rangle}{\partial z} = \mathbf{aM} |\mathbf{S}(z)\rangle, \quad (2)$$

where \mathbf{M} can be identified with a differential Müller matrix to be written

$$\mathbf{M} = \begin{bmatrix} t' & u' & -v' & w \\ u' & t' & -w' & v \\ -v' & w' & t' & u \\ w & -v & -u & t' \end{bmatrix}, \quad (3)$$

with

$$t' = -[\alpha_{xx}(g) + \alpha_{yy}(g)] - [\zeta_{xxz}(g) + \zeta_{yyz}(g)] - [Q_{xzzx}(g) + Q_{yzyy}(g)], \quad (4)$$

$$u = +[\alpha_{xx}(f) - \alpha_{yy}(f)] + [\zeta_{xxz}(f) - \zeta_{yyz}(f)] + [Q_{xzzx}(f) + Q_{yzyy}(f)], \quad (5)$$

$$u' = -[\alpha_{xx}(g) - \alpha_{yy}(g)] - [\zeta_{xxz}(g) - \zeta_{yyz}(g)] - [Q_{xzzx}(g) - Q_{yzyy}(g)], \quad (6)$$

$$v = +2[\alpha_{xy}(f) + \zeta_{xyz}(f) + Q_{xzyy}(f)], \quad (7)$$

$$v' = -2[\alpha_{xy}(g) + \zeta_{xyz}(g) + Q_{xzyy}(g)], \quad (8)$$

$$w = +2[\alpha'_{xy}(g) + \zeta'_{xyz}(g) + Q'_{xzyy}(g)], \quad (9)$$

$$w' = -2[\alpha'_{xy}(f) + \zeta'_{xyz}(f) + Q'_{xzyy}(f)], \quad (10)$$

in which f and g refer to the dispersive and absorptive lineshapes, respectively.

2.2. Analytical formulation of linear and circular dichroisms in biaxial crystals

The integration of (3) allowed us to derive analytical expressions for linear dichroism or circular dichroism in biaxial as well as uniaxial crystals. For an experiment performed in the transmission geometry one would obtain the following expressions for the X-ray natural circular or linear dichroism (up to the second order in d , the crystal thickness): for XNCD,

$$\sigma^L - \sigma^R \simeq \{2(ad)w - (ad)^2[uv' - vu']\}\mathbf{P}_3^0; \quad (11)$$

for XNLD,

$$\sigma^{90^\circ} - \sigma^{0^\circ} \simeq \{2(ad)u' - (ad)^2[vw + v'w']\}\mathbf{P}_1^0, \quad (12)$$

$$\sigma^{135^\circ} - \sigma^{45^\circ} \simeq \{2(ad)v' - (ad)^2[uw + u'w']\}\mathbf{P}_2^0, \quad (13)$$

where \mathbf{P}_1^0 , \mathbf{P}_2^0 and \mathbf{P}_3^0 are the Poincaré–Stokes parameters of the incident radiation. The second-order term in (11) was first discovered by Born (Born & Huang, 1954) with a model which neglected magnetic dipoles ($M1$) and electric quadrupoles ($E2$). It was rediscovered recently by Machavariani (1995) who exploited a different approach. It vanishes for uniaxial crystals since $u = u' = v = v' = 0$. To the best of our knowledge, so far there is no clear experimental evidence that it can be measured. On the other hand, it is well documented from symmetry considerations with respect to the action of the time-reversal operator that neither $\alpha'_{xy}(g)$ nor $Q'_{zz}(g)$ can induce any dichroism unless a magnetic field is applied. This clearly confirms that XNCD in a uniaxial crystal can only be related to the gyrotropy tensor and more specifically to the electric dipole ($E1$) electric quadrupole ($E2$) interference term.

As detailed elsewhere (Goulon *et al.*, 1999b), similar expressions were also derived for Fd-XNCD/XNLD. What is measured here is the difference in the fluorescence intensity emitted in a given direction when the polarization state of the incident radiation is changed from a left-handed circular polarization to a right-handed circular polarization, from a vertical to a horizontal polarization, or from a polarization at 135° to the orthogonal linear polarization at 45° . The quantities of interest are the generalized Stokes parameters: for Fd-XNCD,

$$\mathbf{S}_0^3 \simeq -\frac{2I_0\mathbf{P}_3^0\Gamma_{00}^F}{\cos\varphi} \{w\mu + [t'w + (u'v - uv')]\mu^2\}; \quad (14)$$

for Fd-XNLD,

$$\mathbf{S}_0^1 \simeq -\frac{2I_0\mathbf{P}_1^0\Gamma_{00}^F}{\cos\varphi} \{u'\mu + [t'u' - (vw + v'w')]\mu^2\}, \quad (15)$$

$$\mathbf{S}_0^2 \simeq -\frac{2I_0\mathbf{P}_2^0\Gamma_{00}^F}{\cos\varphi} \{-v'\mu - [t'v' + (uw + u'w')]\mu^2\}, \quad (16)$$

where I_0 is the total incident intensity; Γ_{00}^F characterizes the fluorescence yield and the polarization state of the fluorescence emitted in a direction \mathbf{k}_F defined by its direction cosine $\cos\varphi$ with respect to the incident beam of wave-vector \mathbf{k} . We found also most convenient to define the reduced isotropic absorption coefficient,

$$1/\mu = -[t'_i + t'_F].$$

If one compares (14) and (11), it immediately appears that Fd-XNCD is strictly proportional to XNCD for uniaxial crystals as long as the X-ray beam propagates along the direction of the optical axis. This is no longer true for biaxial crystals because the second-order terms are different. Again, non-gyrotropic crystals with $w = w' = 0$ might exhibit non-zero Fd-XNCD spectra if $uv' - vu' \neq 0$. However, the latter term is competing with another second-order term ($w't'$) which does not exist in transmission XNCD but is proportional to the gyrotropy term which we want to access.

2.3. XNCD in the framework of the multiple-scattering theory

Ab initio simulations of XNCD spectra are helpful in determining the absolute configuration of chiral centres. The theoretical bases for such calculations were established elsewhere (Natoli *et al.*, 1998; Brouder *et al.*, 1999). The formulations of the XANES and XNCD cross sections at the K - or L_1 -absorption edges are, respectively,

$$\sigma_{\text{XANES}}^{E1,E1} = -\frac{2\pi}{3}\alpha_0\omega[D_1]^2\Im\{\tau_{11c,11c}^{00} + \tau_{11s,11s}^{00}\}, \quad (17)$$

$$\sigma_{\text{XNCD}}^{E1,E2} = -\frac{2\pi}{3\sqrt{5}}[\alpha_0\omega]^2[D_1Q_2]\Im\{\tau_{11c,21s}^{00} - \tau_{11s,21c}^{00}\}. \quad (18)$$

These formulations, which are consistent with the generalized optical theorem, require the calculation of the dipole and quadrupole radial integrals D_ℓ and Q_ℓ as well as the calculation of various scattering path operators,

$$\tau_{\ell mc, \ell' m' c}; \quad \tau_{\ell ms, \ell' m' s}; \quad \tau_{\ell mc, \ell' m' s}; \quad \tau_{\ell ms, \ell' m' c},$$

expressed here with real spherical harmonics. The latter operators can be alternatively expanded in series as a sum of multiple-scattering paths resulting in a general formulation of EXAFS if we refer to (17), and of what we may call chiral-EXAFS (χ -EXAFS) if we refer to (18). Let us remind the reader that neither atomic EXAFS nor single-scattering EXAFS can contribute to χ -EXAFS (Natoli *et al.*, 1998; Brouder *et al.*, 1999).

2.4. Further experimental considerations

All experimental data produced in the following section were collected at the ESRF beamline ID12-A, the optical configuration of which has been described elsewhere (Goulon, Rogalev *et al.*, 1998). The standard helical undulator Helios-II was typically used to record the Fd-XNCD spectra of α -LiIO₃ at the various iodine L -edges. Recently, we have completed the commissioning of a new electro-

Table 2

Polarization state of the monochromatic beam when the helicity of the undulator source is flipped from $\{\mathbf{P}_1^u = \mathbf{P}_2^u = 0.28; +\mathbf{P}_3^u = +0.92\}$ to $\{\mathbf{P}_1^u = \mathbf{P}_2^u = 0.28; -\mathbf{P}_3^u = -0.92\}$.

E (P K -edge) = 2150 eV		Bragg angle = 66.87°	
$\mathbf{P}_{1+} = 0.639$	$\mathbf{P}_{1-} = 0.639$	$\mathbf{P}_{2+} = 0.055$	$\mathbf{P}_{2-} = 0.346$
$\mathbf{P}_{3+} = +0.777$	$\mathbf{P}_{3-} = -0.686$		
E (K K -edge) = 3610 eV		Bragg angle = 33.21°	
$\mathbf{P}_{1+} = 0.854$	$\mathbf{P}_{1-} = 0.854$	$\mathbf{P}_{2+} = 0.013$	$\mathbf{P}_{2-} = 0.167$
$\mathbf{P}_{3+} = +0.323$	$\mathbf{P}_{3-} = -0.276$		
E (Ti K -edge) = 4965 eV		Bragg angle = 23.46°	
$\mathbf{P}_{1+} = 0.529$	$\mathbf{P}_{1-} = 0.529$	$\mathbf{P}_{2+} = 0.118$	$\mathbf{P}_{2-} = 0.285$
$\mathbf{P}_{3+} = +0.695$	$\mathbf{P}_{3-} = -0.650$		

magnetic undulator (EMPHU) which offers the advantage to switch more rapidly from a left-handed to a right-handed circular polarization below 4 keV (Rogalev *et al.*, 1999). This new source definitely increased the reliability of our measurements on α -TeO₂ and made it possible to detect tiny gyrotropy signals at the phosphorus K -edge in KTP.

Unfortunately, even though helical undulator sources can produce intense X-ray beams with high circular polarization rates [$0.92 \leq \mathbf{P}_3^u(\text{source}) \leq 0.97$], much of this advantage is often lost in the poor polarization transfer function of a two-crystal monochromator. Since the Müller matrix associated with the monochromator can be calculated very accurately, one can easily deduce the true polarization state of the X-ray beam at the sample.

It appears immediately from Table 2 that reverting the helicity of the photons emitted by the undulator does not simply revert the helicity of the monochromatic beam at the sample, especially whenever the undulator beam contains a significant \mathbf{P}_2^u component, because the latter is severely altered by the monochromator at large Bragg angles. This point has the dramatic consequence that, in the case of biaxial crystals, XNCD or Fd-XNCD measurements are systematically contaminated with a strong linear dichroism signal (Goulon *et al.*, 1999b). This is because what is measured experimentally is

$$[\mathbf{S}_0^3]_{\text{apparent}} = \mathbf{S}_0^3 + 2\varepsilon_2 \mathbf{S}_0^2, \quad (19)$$

if we define $\mathbf{P}_{3\pm} = \pm \mathbf{P}_3^0(1 \pm \varepsilon_3)$ and $\mathbf{P}_{2\pm} = \mathbf{P}_2^0(1 \pm \varepsilon_2)$.

There is no contamination in the case of uniaxial crystals since $\nu' = 0 \rightarrow \mathbf{S}_0^2 \equiv 0$ according to (13). Note that the apparent Fd-XNCD spectra of a biaxial crystal are no longer invariant in a rotation χ around the beam direction because $\mathbf{S}_0^2 \propto \cos 2n(\chi - \chi_0)$.

3. Results

3.1. Fd-XNCD spectra of uniaxial crystals: α -LiIO₃

The absolute configuration of our crystal was consistent with the laevorotatory structure solved by Svensson *et al.* (1983). The [001] optical axis was carefully aligned with the direction of the incident beam. We have reproduced in Figs. 1(a) and 1(b) the Fd-XANES and Fd-XNCD spectra of α -LiIO₃ recorded at the iodine L_{III} - and L_{II} -edges.

The differences were normalized with respect to the corresponding edge jump. The maximum amplitude of the XNCD signal is of the order of 0.3%. The signal-to-noise ratio is not as good at the L_{II} -edge as at the L_{III} -edge as a consequence of the noisy background resulting from all fluorescence channels opened by the L_{III} -edge photoionization. Nevertheless, the remarkable similarity between the L_{III} - and L_{II} -edge XNCD signals (which have exactly the same sign) is in striking contrast with what is usually observed for L -edge X-ray magnetic circular dichroism (XMCD) spectra. Whereas exchange and spin-orbit interactions are the driving terms in XMCD, this is not the case here and this leaves very little space for a residual contribution of the $E1.M1$ terms.

The XANES and XNCD spectra recorded at the iodine L_I -edge are displayed in Figs. 2(a) and 2(b) and are directly compared with MSW simulations. The maximum amplitude of the XNCD signal is 5.5% after proper correction for the polarization transfer of the monochromator. Such a spectacular amplitude is still slightly less than what was predicted by the *ab initio* simulation (7%) but the agreement between experiment and theory is extremely encouraging. Note that the maximum amplitude of the

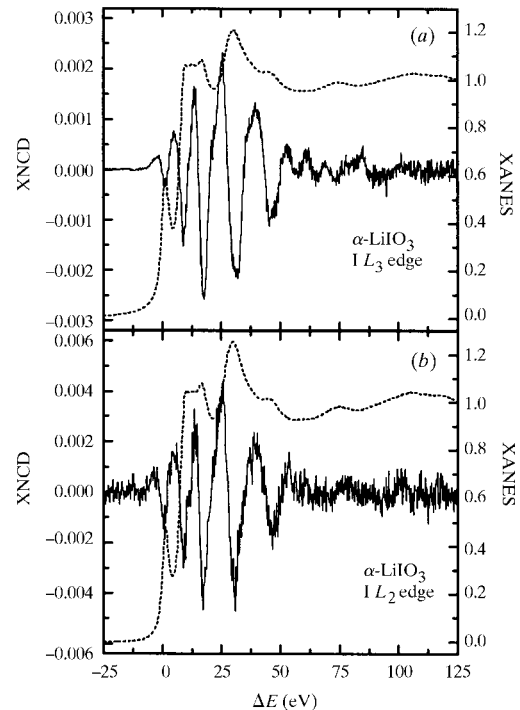


Figure 1
Iodine L_{II-III} -edge Fd-XANES/XNCD spectra of α -LiIO₃.

XNCD is not observed in the very strong white line but for the continuum shape resonances.

3.2. Chiral-EXAFS of paratellurite at the tellurium L_1 -edge

α -TeO₂ is another uniaxial crystal which exhibits a strong XNCD signal at the L_1 -edge of tellurium, as illustrated by Fig. 3(a). Since the spectra were recorded with the new EMPHU source, we were able to detect the Fd-XNCD signal over a wider energy range and EXAFS-like oscillations can be clearly seen. This result prompted us to try to identify which were the multiple-scattering paths contributing most substantially to the XNCD signal. For this specific analysis we used the crystal structure solved by Thomas (1988). As confirmed by the optical FT spectrum reproduced in Fig. 3(b), we found that the chiral paths Te···O₁···O₂···Te involving the nearest oxygen neighbours represent the dominant contribution to the XNCD signal whereas chiral paths of the type Te···Te₁···Te₂···Te or Te···Te₁···O₂···Te have a very broad configurational average spectrum and suffer from a large Debye–Waller damping due to the fact that the Te atoms are heavy and are implicitly associated with low-frequency vibrational modes that are easily populated.

3.3. Fd-XNCD spectra of KTP: the case of biaxial crystals

Given the remarkable applications of KTP in SHG with lasers, the crystal and electronic structures of KTP have

been extensively investigated in recent years (Tordjman *et al.*, 1974; Thomas *et al.*, 1990; Hansen *et al.*, 1991; Ryzhkov *et al.*, 1993). The origin of gyrotropy in this crystal remains nevertheless somewhat ambiguous: (i) the acentric distortion of the Ti sites with one ‘short’ (1.75 Å) and five ‘long’ (2.05 Å) Ti···O bonds is expected to induce gyrotropy; (ii) the pseudo helical distribution of the K⁺ cations with a coordination alternating between 8 and 9 should contribute as well. So far, the symmetric phosphate groups have been assumed to induce no significant gyrotropy.

3.3.1. Titanium and potassium K-edge Fd-XNCD. These time-consuming experiments were performed with the helical undulator Helios-II. This explains why we had to restrict our investigation of the angular dependence of the Fd-XNCD spectra to only four discrete angles (χ_0 ; $\chi_0 + 45^\circ$; $\chi_0 + 90^\circ$; $\chi_0 + 135^\circ$), all measurements being reproduced 12 times. This proved to be enough to disentangle the respective contributions of gyrotropy and linear dichroism as illustrated by Figs. 4 and 5.

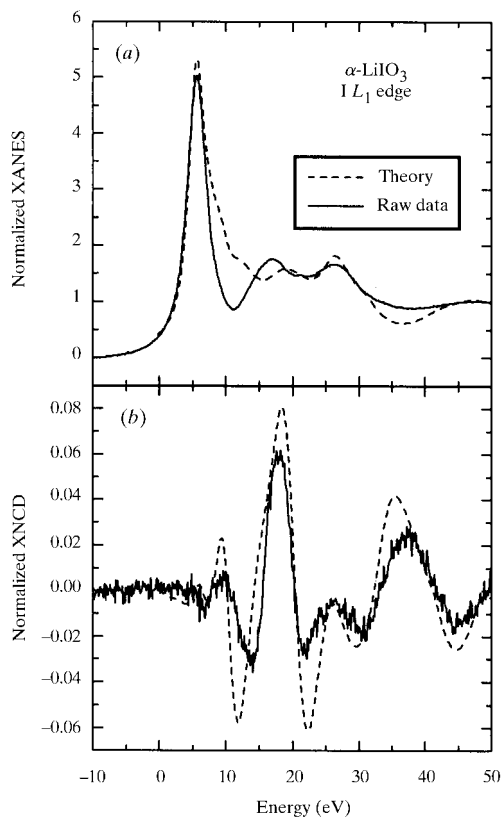


Figure 2 Iodine L_1 -edge Fd-XANES/XNCD spectra: experiment *versus* theory.

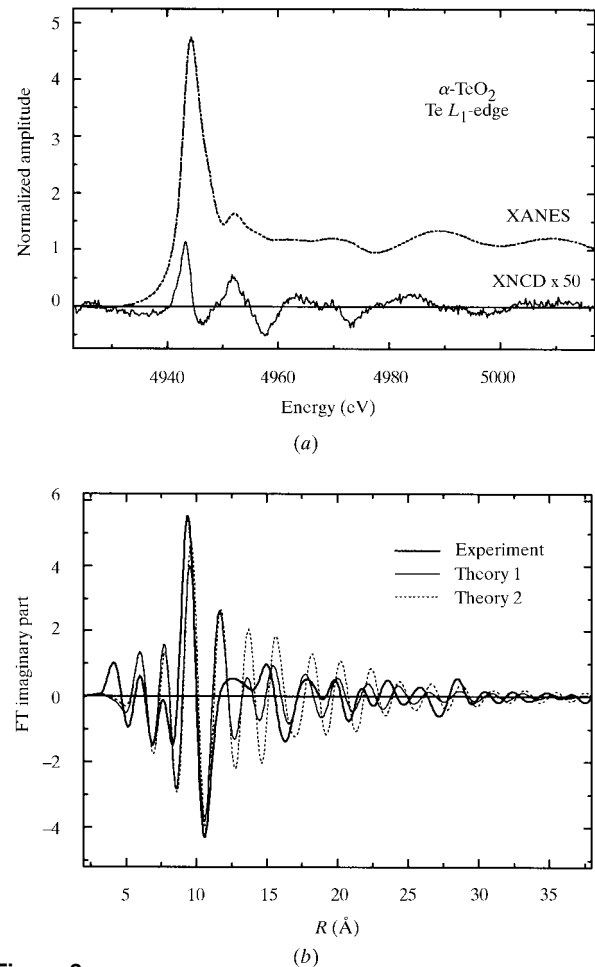


Figure 3 (a) Tellurium L_1 -edge Fd-XANES/XNCD spectra. (b) Optical FT spectra of the Fd-XNCD spectra: experiment *versus* theories. Theory 1 includes only the shortest Te···O₁···O₂···Te chiral paths; theory 2 includes Te···Te₁···Te₂···Te or Te···Te₁···O₂···Te chiral paths as well. All FT spectra were tentatively corrected for the phase and amplitude of the shortest multiple-scattering path.

A nice XNCD signal assigned to X-ray gyrotropy is observed in the pre-edge region of the Ti XANES spectrum and, after proper correction accounting for the polarization transfer function by the monochromator, its maximum amplitude was of the order of 0.45%. This signal was found exactly where the electric quadrupole ($E2$) transitions to d states can be predicted to exhibit the highest amplitude. Also supporting our assignment is the fact that the X-ray gyrotropy signal has the opposite sign for crystals cut parallel to the planes (120) and $(\bar{1}\bar{2}0)$, respectively.

The experiments at the potassium K -edge were more difficult due to the poor polarization transfer of the monochromator. Nevertheless, after correction, the amplitude of the signal assigned to the crystal gyrotropy is of the same order of magnitude (0.5%) but its maximum amplitude is now found beyond the edge.

3.3.2. Spectra recorded at the phosphorus K -edge. The detection of such a small X-ray gyrotropy signal was a formidable challenge which would have probably failed without the advantages offered by the new electromagnetic helical undulator (EMPHU). We have reproduced in Fig. 6(a) the strong linear dichroism signal S_0^2 associated with $n = 2$ in the Fourier decomposition of the apparent Fd-XNCD signal. On the other hand, we have reproduced in Fig. 6(b) the rotational invariant signal associated with X-ray gyrotropy and which is perfectly anticorrelated for measurements performed with crystals cut parallel to the planes (120) and $(\bar{1}\bar{2}0)$, respectively. The maximum amplitude of this X-ray gyrotropy signal would be of the order of 0.1% if one takes into account the polarization transfer of

the monochromator. There is also a weak residual signal (0.05%) which keeps the same sign and the same amplitude for the two crystals: this signal was provisionally assigned to a residual contribution of the second-order term (Goulon *et al.*, 1999, 2000). From the crystal symmetry one would anticipate $[uv' - vu'] = 0$ but this is no longer true if the crystal axis is not strictly parallel to the X-ray beam direction and the residual effect would precisely keep the same sign for crystals cut parallel to the (120) and $(\bar{1}\bar{2}0)$ planes.

4. Conclusion

We have proposed a theory of X-ray gyrotropy for uniaxial or biaxial crystals. It clearly establishes that X-ray absorption spectroscopy can give access to the absolute configuration of chiral structures through the detection of the $E1E2$ interference terms. A major restriction with respect to optical spectroscopy is that these terms vanish in the absence of orientational order. Not only XNCD signals but also χ -EXAFS oscillations can be detected and analysed. The extraction of tiny signals related to X-ray gyrotropy will ever remain a fairly difficult task for biaxial crystals due to the contamination with strong linear dichroism signals. We have shown, however, that a careful Fourier analysis of the angular dependence of the apparent Fd-XNCD spectra recorded for discrete orientations of the crystal rotated around the beam axis is a powerful method of disentangling linear and circular dichroisms. This

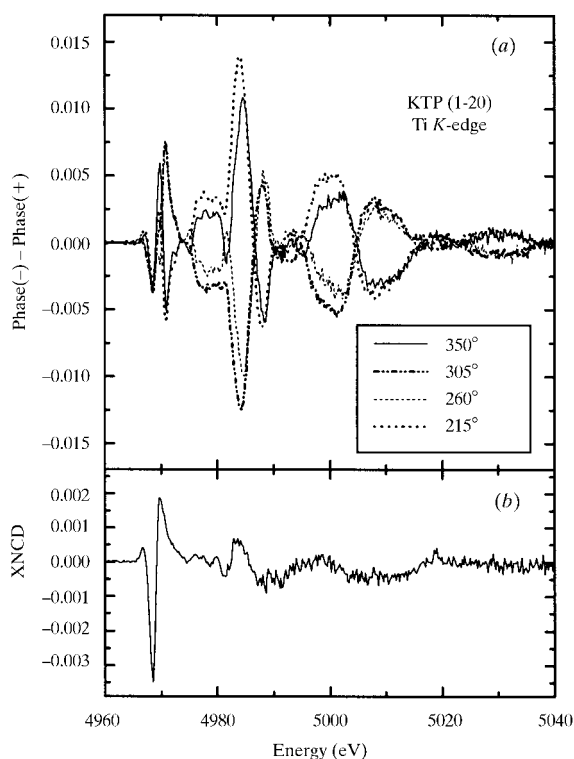


Figure 4
(a) XNLD; (b) X-ray gyrotropy of KTP at the Ti K -edge.

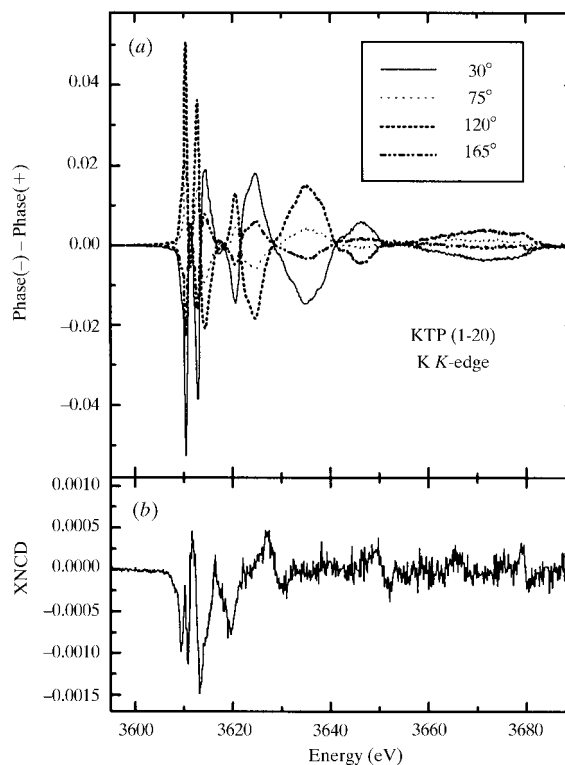


Figure 5
(a) XNLD; (b) X-ray gyrotropy of KTP at the K K -edge.

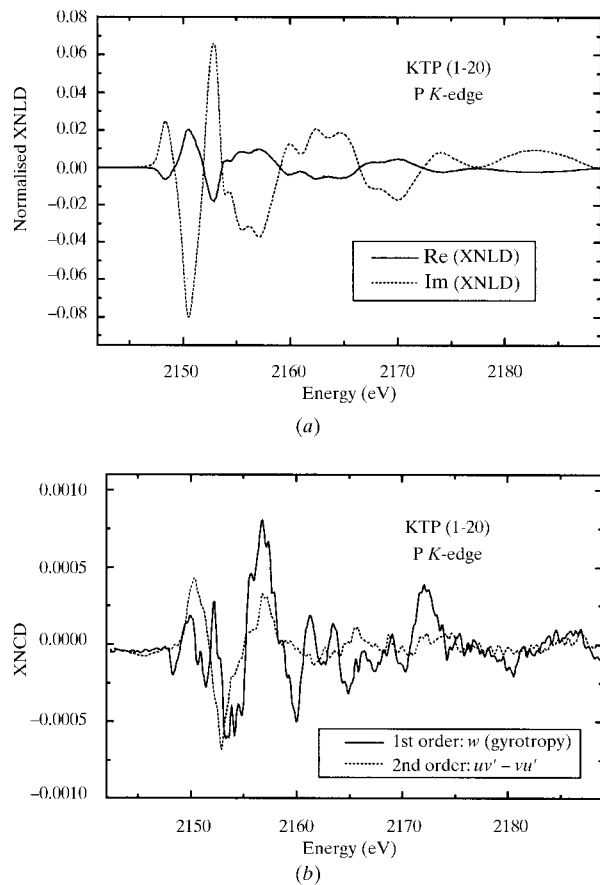


Figure 6

(a) Phosphorus *K*-edge XNLD spectra of the real and imaginary parts of the second Fourier moment. (b) Extracted contributions of X-ray gyrotropy and second-order XNCD of KTP at the phosphorus *K*-edge.

method may offer also the possibility of extracting the second-order circular dichroism term, *i.e.* $[uv' - vu']$, which is existing within the pure electric dipole approximation.

References

Alagna, L., Prosperi, T., Turchini, S., Goulon, J., Rogalev, A., Goulon-Ginet, C., Natoli, C. R., Stewart, B. & Peacock, R. D. (1998). *Phys. Rev. Lett.* **80**, 4799–4802.
 Arago, D.-F.-M. (1811). *Mem. Inst. Fr. (Paris)*, **12**, 93.

Barron, L. D. (1971). *Mol. Phys.* **21**, 241–246.
 Biot, J.-B. (1812). *Mem. Inst. Fr. (Paris)*, **13**, 218.
 Born, M. & Huang, K. (1954). *Dynamical Theory of Crystal Lattices*, pp. 336–38. Oxford: Clarendon.
 Brouder, C., Natoli, C. R., Saintavit, Ph., Goulon, J., Goulon-Ginet, C. & Rogalev, A. (1999). *J. Synchrotron Rad.* **6**, 261–263.
 Cotton, A. (1895). *C. R. Acad. Sci. (Paris)*, **120**, 989–1044.
 Goulon, J. (1990). *Rayonnement Synchrotron Polarisé, Electrons Polarisés et Magnétisme*, edited by E. Beaurepaire, B. Carrière & J. P. Kappler, pp. 333–386. Strasbourg: IPCMS.
 Goulon, J., Goulon-Ginet, C., Rogalev, A., Benayoun, G., Brouder, Ch. & Natoli, C. R. (2000). In preparation.
 Goulon, J., Goulon-Ginet, C., Rogalev, A., Benayoun, G., Malgrange, C. & Brouder, Ch. (1999). *Proc. SPIE*, **3773**, 316–325.
 Goulon, J., Goulon-Ginet, C., Rogalev, A., Gotte, V., Malgrange, C. & Brouder, Ch. (1999a). *J. Synchrotron Rad.* **6**, 673–675.
 Goulon, J., Goulon-Ginet, C., Rogalev, A., Gotte, V., Malgrange, C. & Brouder, Ch. (1999b). *Eur. Phys. J. B*, **12**, 373–385.
 Goulon, J., Goulon-Ginet, C., Rogalev, A., Gotte, V., Malgrange, C., Brouder, Ch. & Natoli, C. R. (1998). *J. Chem. Phys.* **108**, 6394–6403.
 Goulon, J., Rogalev, A., Gauthier, Ch., Goulon-Ginet, Ch., Pasté, S., Signorato, R., Neumann, C., Varga, L. & Malgrange, C. (1998). *J. Synchrotron Rad.* **5**, 232–238.
 Hansen, N. K., Protas, J. & Marnier, G. (1991). *Acta Cryst.* **B47**, 660–672.
 Jerphagnon, J. & Chemla, D. S. (1976). *J. Chem. Phys.* **65**, 1522–1529.
 Machavariani, V. Sh. (1995). *J. Phys. Condens. Matter*, **7**, 5151–5154.
 Natoli, C. R., Brouder, Ch., Saintavit, Ph., Goulon, J., Goulon-Ginet, C. & Rogalev, A. (1998). *Eur. Phys. J. B*, **4**, 1–11.
 Okutani, M., Jo, T. & Carra, P. (1999). *J. Phys. Soc. Jpn*, **68**, 3191–3194.
 Rogalev, A., Goulon, J., Benayoun, G., Elleaume, P., Chavanne, J., Penel, Ch. & Van Vaerenbergh, P. (1999). *Proc. SPIE*, **3773**, 275–283.
 Röntgen, W. C. (1896). *Nature*, **53**, 274.
 Ryzhkov, M. V., Medvedeva, N. I. & Gubanov, V. A. (1993). *Phys. Scr.* **48**, 629–632.
 Stewart, B., Peacock, R. D., Alagna, L., Prosperi, T., Turchini, S., Goulon, J., Rogalev, A. & Goulon-Ginet, C. (1999). *J. Am. Chem. Soc.* **121**, 10233–10234.
 Svensson, C., Albertson, J., Liminga, R., Kvik, Å. & Abrahams, S. C. (1983). *J. Chem. Phys.* **78**, 7343–7352.
 Thomas, P. A. (1988). *J. Phys. C*, **21**, 4611–4627.
 Thomas, P. A., Glazer, A. M. & Watts, B. E. (1990). *Acta Cryst.* **B46**, 333–343.
 Thomas, P. A., Tebbutt, J. & Glazer, A. M. (1991). *J. Appl. Cryst.* **24**, 963–967.
 Tordjman, I., Masse, R. & Guitel, J. C. (1974). *Z. Kristallogr.* **139**, 103–115.